

## DETECTION OF INFALL IN THE PROTOSTAR B335 WITH ALMA

NEAL J. EVANS II<sup>1</sup>, JAMES DI FRANCESCO<sup>2</sup>, JEONG-EUN LEE<sup>3</sup>, JES K. JØRGENSEN<sup>4</sup>, MINHO CHOI<sup>5</sup>, PHILIP C. MYERS<sup>6</sup>,  
DIEGO MARDONES<sup>7</sup>

*Draft version August 23, 2018*

### ABSTRACT

Observations of the isolated globule B335 with ALMA have yielded absorption features against the continuum that are redshifted from the systemic velocity in both HCN and HCO<sup>+</sup> lines. These features provide unambiguous evidence for infall toward a central luminosity source. Previously developed models of inside-out collapse can match the observed line profiles of HCN and HCO<sup>+</sup> averaged over the central 50 AU. At the new distance of 100 pc, the inferred infall radius is 0.012 pc, the mass infall rate is  $3 \times 10^{-6} M_{\odot} \text{ yr}^{-1}$ , the age is  $5 \times 10^4$  years, and the accumulated mass in the central zone is  $0.15 M_{\odot}$ , most of which must be in the star or in parts of a disk that are opaque at 0.8 mm. The continuum detection indicates an optically thin mass (gas and dust) of only  $7.5 \times 10^{-4} M_{\odot}$  in the central region, consistent with only a very small disk mass.

*Subject headings:* ISM: individual objects (B335) – line: profiles – stars: formation

### 1. INTRODUCTION

The idea that stars form from the infall of material from a dense core in a molecular cloud is enshrined in all cartoons of star formation. By **infall**, we mean the inward motion of matter toward a central forming star, driven by self-gravity. While such a picture is attractive theoretically, hard observational evidence of such infall has proven to be elusive.

Most evidence in support of infall has been indirect and depends on comparison of observations of molecular line emission profiles to predictions of calculations that involve complexities of chemistry and excitation, along with assumptions about density, temperature, and velocity fields (Myers et al. 2000).

It was realized early (Leung & Brown 1977) that redshifted absorption against a central continuum source would provide an unambiguous indicator of matter in front (absorption) moving inward (redshifted) toward that source. If the envelope emits at velocities centered on the mean envelope velocity in the spectral line chosen, the result is like an inverse P-Cygni profile (IPC), with emission on the blue side of the central velocity and absorption on the red side. Because the opacity of dust grains increases rapidly with frequency at millimeter and submillimeter wavelengths, absorption will be easier to detect at higher frequencies. Wyrowski et al.

(2012) have taken advantage of this fact to find redshifted absorption features in NH<sub>3</sub> rotational transitions at THz frequencies toward a number of massive star-forming clumps, strongly indicative of inflow of material within the clumps. By **inflow**, we mean general inward motion toward a forming cluster of stars, rather than infall toward a single star. Mottram et al. (2013) also used THz frequencies, together with the fact that gas-phase water reaches substantial abundances only in the warm inner regions, to identify IPCs in several regions of lower mass star formation. One drawback of using water is that one must remove the strong emission from the outflow. That is not a problem for observations of starless cores, and Keto et al. (2015) have used IPCs in water lines to detect subsonic contraction motions in L1544, consistent with those predicted for a quasi-equilibrium Bonner-Ebert sphere.

These studies have used *SOFIA* and *Herschel* observations and thus have spatial resolutions of 16'' to 30''. Another approach is to improve the spatial resolution using interferometers (Choi et al. 1999). Di Francesco et al. (2001) exploited this ability to see inverse P-Cygni profiles toward NGC1333 IRAS4. In that rather complex region, there were suggestions that the absorption arose from resolving out emission in an extended foreground region with a slight velocity offset, rather than in an infalling envelope (Choi et al. 2004). Since this source was one of the few with sufficiently strong continuum emission to observe the effect with earlier interferometers, this technique was largely put on the shelf, “waiting for ALMA.”

We can now use ALMA’s high resolution and sensitivity to observe molecular lines in *absorption* against the continuum emission from the disk or inner envelope. Once detected, absorption observed in a number of lines can be used to study the velocity field of infall and the rate of central mass accumulation. More generally, these data can provide an independent constraint on infall models based solely on emission line profiles. Another advantage of very high spatial resolution is that the outflow region may be excluded, allowing study of

nje@astro.as.utexas.edu

<sup>1</sup> Department of Astronomy, The University of Texas at Austin, 2515 Speedway, Stop C1400, Austin, Texas 78712-1205, U.S.A.; nje@astro.as.utexas.edu

<sup>2</sup> National Research Council of Canada, Herzberg Institute of Astrophysics, 5071 West Saanich Road, Victoria, BC V9E 2E7, Canada

<sup>3</sup> School of Space Research, Kyung Hee University, Yongin-shi, Kyungki-do 449-701, Korea

<sup>4</sup> Centre for Star and Planet Formation, Niels Bohr Institute and Natural History Museum of Denmark, Øster Voldgade 5–7, 1350 Copenhagen K., Denmark

<sup>5</sup> Korea Astronomy and Space Science Institute, 776 Daedeok-daero, Daejeon 305-348, Korea

<sup>6</sup> Harvard-Smithsonian Center for Astrophysics, 60 Garden Street, Cambridge, MA 02138, U.S.A.

<sup>7</sup> Departamento de Astronomía, Universidad de Chile, Casilla 36-D, Santiago, Chile

the higher infall velocities closer to the central source.

The ideal source to test infall models is B335, an isolated, roundish, dark globule (see images in Gálfalk & Olofsson 2007). It was the first source for which kinematic evidence of infall was claimed. Zhou et al. (1993) found a spectral signature in several lines of CS and H<sub>2</sub>CO toward B335. The spectral signature, often called an “asymmetrically blue profile” because the blue peak (from the back of an infalling envelope) is stronger than the red peak (from the front of an infalling envelope), requires particular combinations of density, temperature, abundance, and velocity fields, which may not be realized in a given source (see, e.g., Choi et al. 1995). Later, follow-up observations with higher resolution raised doubts about the infall interpretation because of contributions to emission from outflowing gas (Wilner et al. 2000). The recently revised distance to B335 of  $105 \pm 15$  pc (Olofsson & Olofsson 2009) makes it even more attractive for a close-up look. We take a distance of 100 pc, 0.25 times the distance assumed in the past, for convenience. As a result, the observed luminosity is  $0.72 L_{\odot}$ . Finally, the outflow (Hirano et al. 1988) is nearly perpendicular to the line of sight, with an inclination angle of  $87^{\circ}$  (Stutz et al. 2008).

Evans et al. (2005) developed detailed models of line spectra toward B335 available at that time, using inside-out (Shu 1977) infall models and chemical modeling. Recent studies of B335 (Yen et al. 2011, 2010) have confirmed the results of earlier models that found B335 to be a very slowly rotating core in the inner regions. A detailed model of infall was developed by Kurono et al. (2013). Most recently, Yen et al. (2015a) fitted data from the SMA to a model of essentially pure infall, with an upper limit on specific angular momentum in the inner regions of  $j < 5 \times 10^{-5}$  km s<sup>-1</sup>pc, and they predicted that a rotationally supported disk would have a radius no larger than 5 AU. Yen et al. (2015b) have confirmed the slow rotation with ALMA data on C<sup>18</sup>O and SO and set an upper limit of 10 AU on the radius of any Keplerian disk.

## 2. OBSERVATIONS

Observations of B335 were obtained as part of project 2012.1.00346.S (PI. N. Evans) on 27 April 2014 (UT) in the C32-3 configuration of ALMA Early Science. The observations used 35 12-m antennas and the Band 7 receivers. The weather conditions during the observations were reasonable, with roughly stable values of precipitable water vapor ranging between 1.0 mm and 1.1 mm. Data of B335 were obtained over a baseline range of 18.69 m to 527.57 m. Half the flux of a Gaussian with FWHM size of  $4''.1$  would be recovered with this minimum baseline (eq. A8 of Wilner & Welch 1994).

The ALMA Correlator was configured to have four spectral windows (spws), each with 3840 channels 61.035 kHz ( $\sim 0.05$  km s<sup>-1</sup>) wide and a total useable bandwidth of 234.375 MHz. (The spectral resolution is twice the channel width.) The local oscillator was tuned appropriately so that HCN 4-3, HCO<sup>+</sup> 4-3, CS 7-6, and H<sup>13</sup>CN 4-3 could be observed in spws 0, 1, 2, and 3, respectively. The rest frequencies, velocity resolutions, upper state energies above ground (in kelvin), and Einstein  $A_{ul}$  values are given in Table 1.

The execution block lasted for 97 minutes total, and consisted of a  $\sim 10$  minute integration on J1924-2914 to calibrate the bandpass shape of each spw, then a  $\sim 2.5$  minute integration on J1751+096 to calibrate amplitudes. Observations of B335 were obtained with  $\sim 7$  minute integrations and were interleaved with  $\sim 1.5$  minute integrations of J1955+1358 to calibrate phases. B335 was observed for a total of 48.35 minutes. The data were initially calibrated and imaged by staff at the North American ALMA Science Center (NAASC), using standard procedures in the Common Astronomy Software Applications (CASA) package. Passing the QA2 quality assurance step, the data were delivered to the project team for further calibration and imaging, again using CASA.

Preliminary imaging of the NAASC-calibrated data of B335 revealed obvious detections of the continuum source in every channel. A smoothed version of the data was self-calibrated using line-free channels to create a continuum dataset. The data were self-calibrated in phase first at 600 sec intervals followed by another self-calibration in phase at 60 sec intervals. The data were then self-calibrated in amplitude over 3600 sec intervals. All three self-calibrations were then applied to the unsmoothed dataset. A continuum image was then produced by inverting the line-free channels into a field with  $512 \times 512$  cells of  $0''.1 \times 0''.1$  size each, using multi-frequency synthesis to populate the  $uv$ -plane. The dirty image was CLEANed using the basic Clark algorithm down to a threshold of 0.5 mJy, roughly  $2 \sigma$ . The resolution of the CLEAN continuum image was  $0''.486 \times 0''.439$ , P.A. =  $-76.9^{\circ}$ . The line data cubes were then produced by inverting each spectral window with 61.035 kHz channels, respectively, with each channel having the same cell and field sizes as the continuum image. Each channel was also CLEANed using the Clark algorithm down to a threshold of 60 mJy per channel, again  $\sim 2 \sigma$ . The angular resolutions of the CLEAN datacubes were similar to that of the continuum image. The continuum and line data were corrected for primary beam attenuation. Continuum subtraction in the  $uv$  plane can cause artifacts in the presence of absorption features, so we removed the continuum in the image plane. Using MIRIAD (Sault et al. 1995), a continuum signal determined by fitting a polynomial to line-free channels was subtracted from the line data in the image plane. The polynomials were first-order for the HCO<sup>+</sup>, HCN, and CS cubes, but zeroth-order for the H<sup>13</sup>CN cube due to an abundance of lines in that spectrum. The data were then written out as FITS files for further analysis.

## 3. RESULTS

The ALMA data show a very compact continuum source at 350 GHz (Fig. 1). A two-dimensional Gaussian fit yields a source centered at 19:37:00.894, +07:34:09.59 (J2000), with a deconvolved size (FWHM) of  $0''.45$  by  $0''.25$  at position angle of  $10^{\circ}$ , nearly orthogonal to the beam and to the outflow axis. The total flux density is  $91 \pm 6$  mJy. There is also a faint, arc-like structure curving to the east, but appearing to wrap around the continuum source. Jørgensen et al. (2007) found a continuum source at 0.8 mm at 19:37:00.91, +07:34:09.6 (J2000), with a size of  $1''.6$ , and a total flux density of 350 mJy. If this source had been uniform over their source size, we

would have observed 34 mJy into our  $0''.5$  beam, whereas we actually observed 91 mJy, indicative of a very compact structure. At 100 pc, the structure would be 45 AU by 25 AU. This structure is most plausibly the inner part of the infalling envelope. Yen et al. (2015b) provide more detailed analysis of continuum data at similar resolution, obtained at lower frequencies, and they also identify similar structures with comparable mass at this scale. No other compact source is present in the field down to a limit of 6 mJy ( $3\sigma$ ).

The spectral data show very compact (nearly point-like) emission centered on the continuum peak, except near the systemic velocity of  $8.30 \pm 0.05 \text{ km s}^{-1}$  (Evans et al. 2005), where arc-shaped structures can be seen in the CS line, more faintly in the  $\text{HCO}^+$  line, and very faintly in the HCN line. These structures are plausibly the edges of outflow cavities. Channel maps were created after an additional Hanning smoothing to an effective resolution of  $0.2 \text{ km s}^{-1}$ . The channel maps, spaced by about  $0.5 \text{ km s}^{-1}$ , are shown in Figure 2 for  $\text{HCO}^+$  and Figure 3 for HCN. The  $\text{HCO}^+$  emission in the line wings, and absorption at  $8.5 \text{ km s}^{-1}$ , are both compact and centered on the continuum source (half-power emission ellipse shown as a black contour), with no evidence of emission from the outflow. At velocities near the line peaks, the emission is extended, roughly north-south, and separated emission, most likely from the cavity walls of the outflow, can be seen about  $3''.5$  to the northeast and southwest. False absorption can be seen inside the outflow cavities, due to resolved out emission from the cavity walls, at the line peak velocities, but **not** at the velocity of the absorption feature seen toward the continuum source. The channel maps for HCN (Figure 3) are similar to those for  $\text{HCO}^+$ , except that the emission from the cavity walls is apparent only for the channel near the blue peak at  $8.0 \text{ km s}^{-1}$ , and the absorption at  $8.5 \text{ km s}^{-1}$  is less significant.

The spectra for all four lines, extracted from a  $0''.5$  by  $0''.5$  box centered on the continuum source, are shown in Figure 4. Except possibly for CS, contamination by emission from the outflow cavity is negligible in this box. The data were converted to a  $T_R$  scale using conversions from Jy/beam to K for a beam equivalent to the extraction box; sensitivity values are given in Table 1.

The  $\text{HCO}^+$  and HCN spectra show red-shifted absorption, in addition to the stronger blue peak, as predicted for an infall model. The CS spectrum shows a stronger blue peak and red-shifted **self**-absorption, but does not absorb below the continuum. The  $\text{H}^{13}\text{CN}$  spectrum shows no absorption feature.

## 4. MODELS

### 4.1. General Considerations

Unlike earlier observations with lower resolution, these observations provide essentially a pencil beam toward the center of B335, allowing ‘‘Doppler tomography.’’ The different parts of the line profile probe different radii with a minimal mixture of off-center emission. A velocity field  $v(r) \propto r^{-0.5}$  is expected in the innermost regions for an inside-out collapse model. We see no evidence of the outflow at high velocity in the spatial images, so the line wings probe the inner part of the infall. The gas at the ambient velocity lies in the outer, static envelope, while

the gas at low offsets from the ambient velocity probes the outer, but infalling shells.

A line with a high critical or effective density (e.g., Evans 1999; Shirley 2015) will have an optical depth profile that peaks strongly at the radius where the infall velocity is the absolute value of the offset from the line centroid, **if** there is sufficient density at that point in the cloud to excite molecules to that level. With both density and temperature increasing inward, these lines will tend to emit strongly at velocities displaced from the centroid velocity. If the transition is optically thin throughout the shell, the resulting line profile will be double peaked with neither emission nor absorption of the continuum at the line center. A more opaque line will show the classic blue asymmetry, in which the blue peak is stronger, with a minimum of emission at the line center (e.g., the CS  $J = 7 \rightarrow 6$  line). If there is sufficient optical depth in the outer layers, a line observed toward the continuum peak will show absorption against the continuum at the velocity centroid from the static envelope and at redshifted velocities from the outer, infalling shells (e.g., the HCN and  $\text{HCO}^+$   $J = 4 \rightarrow 3$  lines). These features can be seen in models with simple abundance distributions (§4.2).

Another possible cause for an absorption dip that is redshifted from the mean core velocity is an unrelated, redshifted foreground layer, as was suggested in the case of NGC1333 IRAS4 (Choi et al. 2004). The simplicity and isolation of the B335 globule (G alfalk & Olofsson 2007) make this explanation highly unlikely, and no evidence for such a layer is seen in the many spectra of the source in Evans et al. (2005) nor in the maps of the region in Stutz et al. (2008). Furthermore, the lower states of the lines observed here lie much higher in energy than those observed in NGC1333 IRAS4, requiring a warm, dense layer to provide significant optical depth. The excellent coverage of the uv plane with ALMA, together with the lack of any foreground molecular gas in B335, largely eliminates the concerns expressed about the interpretation of the redshifted absorption toward the NGC1333 region.

To demonstrate further that the absorption feature is confined to the continuum source, we averaged spectra extracted in circles of  $0''.5$  diameter located  $0''.5$  north and south of the center, avoiding the outflow which goes east and west. These are shown in Figure 5. While red-shifted **self**-absorption can be seen, the lines no longer show significant absorption below the continuum. (The  $\text{HCO}^+$  line does go slightly below the continuum, but only at the  $2\sigma$  level.)

Taken together, these facts indicate that infall has been clearly detected in the HCN and  $\text{HCO}^+$  lines via the IPC signature. This conclusion is the most important result and is independent of the following, more detailed modeling.

### 4.2. Simple Models of Line Emission: Pure Infall

Our goal is to see if a previously developed physical model can account approximately for the observed line profiles. More complex models, with asymmetric structures and outflow cavities, require other constraining data, and are deferred to a later paper. Because the HCN and  $\text{HCO}^+$  line profiles both show red-shifted absorption, we focus on them here.

The basic physical model is the inside-out collapse

model (Shu 1977), in which a wave of infall propagates outward at the effective sound speed ( $c_{s,\text{eff}}$ ), which is the quadrature sum of thermal and turbulent contributions. With  $c_{s,\text{eff}}$  constrained by observations, the model has only one free parameter, the time since collapse began ( $t$ ), or equivalently the infall radius ( $r_{\text{infall}}$ ) because  $r_{\text{infall}} = c_{s,\text{eff}}t$ . Outside the infall radius ( $r_{\text{infall}}$ ), the infall velocity is zero; inside  $r_{\text{infall}}$ , the infall velocity increases as  $r$  decreases ( $v \propto r^{-0.5}$ ) and the density distribution is more shallow. The size of  $r_{\text{infall}}$  is the best free parameter for comparison to observations.

We use the same modeling apparatus as we used in Evans et al. (2005). Details are given there, but we summarize them here briefly. A model of inside-out collapse is calculated from the equations in Shu (1977), assuming an initial  $T_K = 13$  K (Zhou et al. 1990), a dust radiative transport code calculates the dust temperature as a function of radius, and a gas energetics code calculates the gas temperature as a function of radius including photoelectric and cosmic ray heating, molecular line cooling, and energy transfer between dust and gas (Young et al. 2004). To this physical model, we add a distribution of molecular abundance for the species being modeled, calculate the level populations with a Monte Carlo code for line radiative transfer (Choi et al. 1995), and calculate the line profile into a beam of diameter  $0''.57$  to match the area of the extraction box for the spectra. To model the source on smaller scales to match the finer resolution of the ALMA observations, we have doubled the number of shells (to 80) in the radiative transport code, extending the inner radius of the model to 6 AU. We have added a continuum source at the center of the model, using the continuum flux density, converted to radiation temperature. Once the excitation and radiative transport have been calculated, we remove a baseline using velocities outside the range of emission to produce the model spectra because the continuum was subtracted from the data. Thus absorption against the continuum will go below zero in the models, as well as in the observations.

Based on optimizing the fit to many lines observed with resolutions ranging from  $16''$  to  $89''$ , Evans et al. (2005) confirmed the best-fit infall radius found by Choi et al. (1995), after scaling to the new distance of 100 pc, of  $r_{\text{infall}} = 0.012$  pc. Similarly, the luminosity is scaled down to  $0.72 L_{\odot}$  at the new distance. The ALMA data for HCN and  $\text{HCO}^+$  and the predictions of the model with  $r_{\text{infall}} = 0.012$  pc are shown in Figure 5. The model produces a reasonably good fit to the double-peaked lines, the absorption dip, and even the line wings. Models of the off-source spectra (right panels in Figure 5) are also reasonably close to the observations; they show self-absorption, but no absorption against the continuum (a weak continuum, measured from the observations, of about 10 mJy/beam was included in the model). These features of both observations and models match the expectations for line models discussed in §4.1. The simple, spherical models do not perfectly match the observations. More flexible models with flattened envelopes, outflow cavities, etc. will be explored in future work.

Tests of other infall radii clearly confirm the value of  $r_{\text{infall}}$  from Evans et al. (2005). Smaller infall radii fail to predict the width of the red-shifted absorption and the wings of the lines. Larger infall radii predict absorption features and line wings that are wider than observed.

This  $r_{\text{infall}}$  is also consistent with the broken power-law model of Kurono et al. (2013), who find a break at 0.013 pc, after adjustment from their assumed distance of 150 pc to our assumed distance of 100 pc.

The abundances of the molecules needed tuning on small scales to match the data. For the  $\text{HCO}^+$  line, we used a step function abundance profile, in which the abundance drops inside a radius  $r_{\text{out}}$ . For the HCN line, a drop function (Jørgensen et al. 2004) was used, in which the abundance drops inside  $r_{\text{out}}$ , but rises again within  $r_{\text{in}}$ . Parameters for both are shown in Table 2. While often used, these abundance models are somewhat ad hoc and we present them only as a proof of principle that the absorption feature and the line profile in general can be matched.

The fact that the observed spectra, including both the redshifted dip and the line wings, can be fitted with a simple model of inside-out collapse, with  $r_{\text{infall}}$  determined from data on much larger angular scales, albeit with ad hoc abundance variations, gives us further confidence in our interpretation of the observations as a clear detection of infall.

#### 4.3. Updated Model and Uncertainties

In this section, we update the parameters of the infall model of Evans et al. (2005) to reflect the distance of 100 pc and discuss some uncertainties in the parameters. The infall radius of 0.012 pc, together with an effective sound speed (combining thermal and turbulent contributions) of  $c_{s,\text{eff}} = 0.233$  km s $^{-1}$ , implies an age of  $5.0 \times 10^4$  years since formation of the central point source, reasonably consistent with the dynamical timescale for the outflow of  $3 \times 10^4$  years (adjusted to 100 pc) from Stutz et al. (2008). The mass infall rate would be  $\dot{M}_{\text{infall}} = 0.975c_s^3/G = 2.94 \times 10^{-6} M_{\odot} \text{ yr}^{-1}$ , allowing a central mass (star and disk) of  $0.15 M_{\odot}$  to accumulate if the infall rate has been constant and mass loss in the wind is neglected.

For comparison, the mass of gas and dust inside a radius of 25 AU can be estimated from the continuum emission of 91 mJy, using equation A.31 of Kauffmann et al. (2008). This quantity is the mass that is not opaque at  $846 \mu\text{m}$ , so it does not measure mass in a star or the opaque part of a disk. We use the mass-weighted dust temperature (equation 8) of Kauffmann et al. (2008) of 111 K, based on the model dust temperature of 67 K at 25 AU. Finally, we use the average opacity at  $850 \mu\text{m}$  determined for B335 itself by Shirley et al. (2011) of  $1.48 \times 10^{-2}$  cm $^2$  per gram of gas for a gas to dust ratio of 100. The resulting mass is  $7.5 \times 10^{-4} M_{\odot}$ , much less than the  $0.15 M_{\odot}$  that has fallen in, indicating that most of the accumulated central mass is probably in the forming star. Yen et al. (2015b) fit their  $\text{C}^{18}\text{O}$  data with a smaller central mass,  $0.05 M_{\odot}$ ; this small a mass is not compatible with the line wings that we observe. The limit on other continuum sources in the field translates to  $5 \times 10^{-5} M_{\odot}$ , ensuring that B335 remains single on scales of 100 - 1000 AU.

The mass infall rate can be compared to the rate of accretion onto the central star ( $\dot{M}_{\text{acc}}$ ) and to the mass loss rate in the wind ( $\dot{M}_{\text{w}}$ ) with several further assumptions.

$$\dot{M}_{\text{acc}} = \frac{L_{\star} R_{\star}}{GM_{\star} f_{\text{acc}}}, \quad (1)$$

where  $L_*$  is the stellar luminosity,  $R_*$  is the stellar radius,  $G$  is the gravitational constant,  $M_*$  is the stellar mass, and  $f_{\text{acc}}$  is the radiative efficiency of accretion (e.g., equation 2 of Dunham et al. 2014, where we neglect the photospheric luminosity). Radiative transfer models of aspherical clouds with outflows oriented nearly perpendicular to the line of sight show that observed luminosities can underestimate the actual luminosity by substantial factors (e.g., Natta et al. 1981; Whitney et al. 2003; Offner et al. 2012). Preliminary models of B335 with outflow cavities suggest that the actual luminosity is about twice the observed luminosity, so we take  $L_* = 1.5 L_\odot$ . If all the mass that has fallen in so far is in the star,  $M_* = 0.15 M_\odot$ . The value of  $f_{\text{acc}}$  is probably less than 0.5, while the value of  $R_*$  depends on the mode of accretion (Baraffe et al. 2012). If we take  $f_{\text{acc}} = 0.5$  and  $R_* = 1.5 R_\odot$ , we get  $\dot{M}_{\text{acc}} = 9.6 \times 10^{-7} M_\odot \text{ yr}^{-1}$ , about one-third of the infall rate. Like many other young objects, B335 may have a lower current accretion rate than infall rate, evidence for episodic accretion models (Dunham et al. 2014).

The time-averaged mass loss rate in the wind,  $\dot{M}_w$ , can be inferred from the force needed to drive the CO outflow divided by the wind velocity. Scaling the force given by Cabrit & Bertout (1992) to a distance of 100 pc yields a value of  $1.4 \times 10^{-5} M_\odot \text{ yr}^{-1} \text{ km s}^{-1}$ . For a wind velocity of  $100 \text{ km s}^{-1}$ ,  $\dot{M}_w = 1.4 \times 10^{-7} M_\odot \text{ yr}^{-1}$ , 7 times less than the accretion rate inferred from the current luminosity. A factor of 10 is commonly assumed.

Comparison of all these rates suggests that the current accretion rate is not dramatically different from its time-averaged value, but that it is less than the infall rate. If mass is accumulating somewhere besides the star, it cannot be in the optically thin parts of a disk. A magnetically supported pseudo disk is an interesting possibility in light of the evidence for magnetic braking (Yen et al. 2015b).

The model used here, spherical inside-out collapse from an isothermal sphere, is very simple. Because it fits the data well, it makes no sense to use a more complex models, with more free parameters, to analyze these data. However, we discuss briefly the likely effect of some more complex models. Dense cores are known to have temperature gradients, with  $T$  as low as 7-8 K near the center (e.g., Evans et al. 2001; Crapsi et al. 2007; Launhardt et al. 2013). A temperature gradient changes the pre-collapse density structure, but the effects are modest (Evans et al. 2001). Also, the infall wave would propagate more slowly at early times, but this effect is mitigated by the turbulent contribution to the effective sound speed. Assuming a constant  $T_K$  of 8 K, rather than 13 K, would make the age  $6.1 \times 10^4 \text{ yr}$ , about 20% larger. The initially lower  $T_K$  would also be counteracted by the heating of the interior by the growing stellar luminosity.

The mass infall rate and central mass are more sensitive to the sound speed ( $\dot{M}_{\text{inf}} \propto c_{s,\text{eff}}^3$  and  $M_* \propto c_{s,\text{eff}}^2$ , respectively). An initial temperature of 8 K would yield  $\dot{M}_{\text{inf}} = 1.6 \times 10^{-6} M_\odot \text{ yr}^{-1}$  and  $M_* = 0.097 M_\odot$ . Interestingly, experiments with initial temperatures even as low as 10 K produced worse fits to the HCN line.

Rotation will modify the evolution, but other studies have shown that B335 has very little rotation even at small scales, probably because of magnetic braking (Yen et al. 2015b). The most important complication is the existence of the outflow, which can cause an underestimate of the luminosity and hence temperature of the gas. More direct effects, such as confusing the infall signature with outflow emission, seem to be unimportant at the resolution of these observations.

## 5. SUMMARY

The HCO<sup>+</sup> and HCN lines observed with 0''.5 resolution by ALMA show red-shifted absorption, as expected for a model of infalling gas. A model of infall from a singular isothermal sphere developed previously from data with much lower spatial resolution can fit the new data, when updated with the much closer distance and with some tuning of abundances. B335 is clearly a special source in that it is isolated and close to us. However, it fits in, toward the low luminosity end, with a group of very embedded sources found recently; from the fraction of all protostars in this phase Stutz et al. (2013) estimated a lifetime of  $2.5 \times 10^4 \text{ yr}$ , comparable to what we find for B335 with a completely different method. Further studies of this source can shed light on the larger class of very young protostars.

We are grateful to A. Stutz and H-W. Yen for comments on a previous version. This paper makes use of the following ALMA data: ADS/JAO.ALMA#2012.1.00346.S. ALMA is a partnership of ESO (representing its member states), NSF (USA) and NINS (Japan), together with NRC (Canada) and NSC and ASIAA (Taiwan), in cooperation with the Republic of Chile. The Joint ALMA Observatory is operated by ESO, AUI/NRAO and NAOJ. This work was supported by NSF grant AST-1109116 to the University of Texas at Austin. The research of JKJ is supported by a Lundbeck Foundation Junior Group Leader Fellowship. J.-E. Lee was supported by the Basic Science Research Program through the National Research Foundation of Korea (NRF) (grant No. NRF-2015R1A2A2A01004769) and the Korea Astronomy and Space Science Institute under the R&D program (Project No. 2015-1-320-18) supervised by the Ministry of Science, ICT and Future Planning.

## REFERENCES

- Baraffe, I., Vorobyov, E., & Chabrier, G. 2012, *ApJ*, 756, 118  
 Cabrit, S., & Bertout, C. 1992, *A&A*, 261, 274  
 Choi, M., Evans, II, N. J., Gregersen, E. M., & Wang, Y. 1995, *ApJ*, 448, 742  
 Choi, M., Kamazaki, T., Tatematsu, K., & Panis, J.-F. 2004, *ApJ*, 617, 1157  
 Choi, M., Panis, J.-F., & Evans, II, N. J. 1999, *ApJS*, 122, 519  
 Crapsi, A., Caselli, P., Walmsley, M. C., & Tafalla, M. 2007, *A&A*, 470, 221  
 Di Francesco, J., Myers, P. C., Wilner, D. J., Ohashi, N., & Mardones, D. 2001, *ApJ*, 562, 770  
 Dunham, M. M., Stutz, A. M., Allen, L. E., et al. 2014, *Protostars and Planets VI*, 195  
 Evans, N. J., II 1999, *ARA&A*, 37, 311  
 Evans, II, N. J., Lee, J.-E., Rawlings, J. M. C., & Choi, M. 2005, *ApJ*, 626, 919  
 Evans, N. J., II, Rawlings, J. M. C., Shirley, Y. L., & Mundy, L. G. 2001, *ApJ*, 557, 193  
 Gálfalk, M. & Olofsson, G. 2007, *A&A*, 475, 281

- Hirano, N., Kameya, O., Nakayama, M., & Takakubo, K. 1988, *ApJ*, 327, L69
- Jørgensen, J. K., Bourke, T. L., Myers, P. C., et al. 2007, *ApJ*, 659, 479
- Jørgensen, J. K., Schöier, F. L., & van Dishoeck, E. F. 2004, *A&A*, 416, 603
- Kauffmann, J., Bertoldi, F., Bourke, T. L., Evans, II, N. J., & Lee, C. W. 2008, *A&A*, 487, 993
- Keto, E., Caselli, P., & Rawlings, J. 2015, *MNRAS*, 446, 3731
- Kurono, Y., Saito, M., Kamazaki, T., Morita, K.-I., & Kawabe, R. 2013, *ApJ*, 765, 85
- Launhardt, R., Stutz, A. M., Schmiedeke, A., et al. 2013, *A&A*, 551, A98
- Leung, C. M. & Brown, R. L. 1977, *ApJ*, 214, L73
- Mottram, J. C., van Dishoeck, E. F., Schmalzl, M., et al. 2013, *A&A*, 558, A126
- Myers, P. C., Evans, II, N. J., & Ohashi, N. 2000, *Protostars and Planets IV*, 217
- Natta, A., Palla, F., Preite-Martinez, A., & Panagia, N. 1981, *A&A*, 99, 289
- Offner, S. S. R., Robitaille, T. P., Hansen, C. E., McKee, C. F., & Klein, R. I. 2012, *ApJ*, 753, 98
- Olofsson, S. & Olofsson, G. 2009, *A&A*, 498, 455
- Sault, R. J., Teuben, P. J., & Wright, M. C. H. 1995, in *Astronomical Society of the Pacific Conference Series*, Vol. 77, *Astronomical Data Analysis Software and Systems IV*, ed. R. A. Shaw, H. E. Payne, & J. J. E. Hayes, 433
- Shirley, Y. L. 2015, *PASP*, 127, 299
- Shirley, Y. L., Huard, T. L., Pontoppidan, K. M., et al. 2011, *ApJ*, 728, 143
- Shu, F. H. 1977, *ApJ*, 214, 488
- Stutz, A. M., Rubin, M., Werner, M. W., et al. 2008, *ApJ*, 687, 389
- Stutz, A. M., Tobin, J. J., Stanke, T., et al. 2013, *ApJ*, 767, 36
- Whitney, B. A., Wood, K., Bjorkman, J. E., & Wolff, M. J. 2003, *ApJ*, 591, 1049
- Wilner, D. J., Myers, P. C., Mardones, D., & Tafalla, M. 2000, *ApJ*, 544, L69
- Wilner, D. J. & Welch, W. J. 1994, *ApJ*, 427, 898
- Wyrowski, F., Güsten, R., Menten, K. M., Wiesemeyer, H., & Klein, B. 2012, *A&A*, 542, L15
- Yen, H.-W., Koch, P. M., Takakuwa, S., et al. 2015a, *ApJ*, 799, 193
- Yen, H.-W., Takakuwa, S., Koch, P. M., et al. 2015b, *arXiv:1509.04675*
- Yen, H.-W., Takakuwa, S., & Ohashi, N. 2010, *ApJ*, 710, 1786
- Yen, H.-W., Takakuwa, S., & Ohashi, N. 2011, *ApJ*, 742, 57
- Young, K. E., Lee, J.-E., Evans, II, N. J., Goldsmith, P. F., & Doty, S. D. 2004, *ApJ*, 614, 252
- Zhou, S., Evans, N. J., II, Butner, H. M., et al. 1990, *ApJ*, 363, 168
- Zhou, S., Evans, II, N. J., Koempe, C., & Walmsley, C. M. 1993, *ApJ*, 404, 232

TABLE 1  
ALMA OBSERVATIONS

Transition	Frequency (GHz)	$\delta v$ (km s <sup>-1</sup> )	$E_u$ (K)	$A_{ul}$ (s <sup>-1</sup> )	Sensitivity (K/(Jy/bm) <sup>-1</sup> )
CS $J = 7 \rightarrow 6$	342.882860	0.107	65.8	$8.4 \times 10^{-4}$	32.0
H <sup>13</sup> CN $J = 4 \rightarrow 3$	345.339760	0.106	41.4	$1.90 \times 10^{-3}$	31.6
HCN $J = 4 \rightarrow 3$	354.505470	0.103	42.5	$2.05 \times 10^{-3}$	30.0
HCO <sup>+</sup> $J = 4 \rightarrow 3$	356.734240	0.103	42.8	$3.57 \times 10^{-3}$	29.6

TABLE 2  
MOLECULAR ABUNDANCES

Species	$X$	$X_{\text{drop}}$	$r_{\text{out}}$ (pc)	$r_{\text{in}}$ (pc)
HCO <sup>+</sup>	$3.0 \times 10^{-9}$	$1.5 \times 10^{-10}$	$1.2 \times 10^{-3}$	...
HCN	$1.5 \times 10^{-9}$	$7.5 \times 10^{-11}$	$1.2 \times 10^{-3}$	$1 \times 10^{-4}$

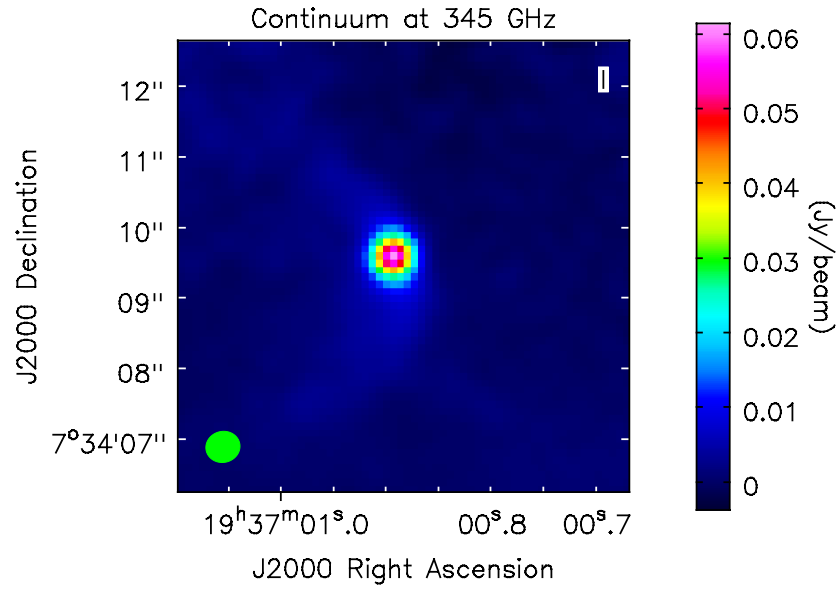


FIG. 1.— Continuum image of B335 at 345 GHz. The beam is shown in the lower left corner as a green ellipse.

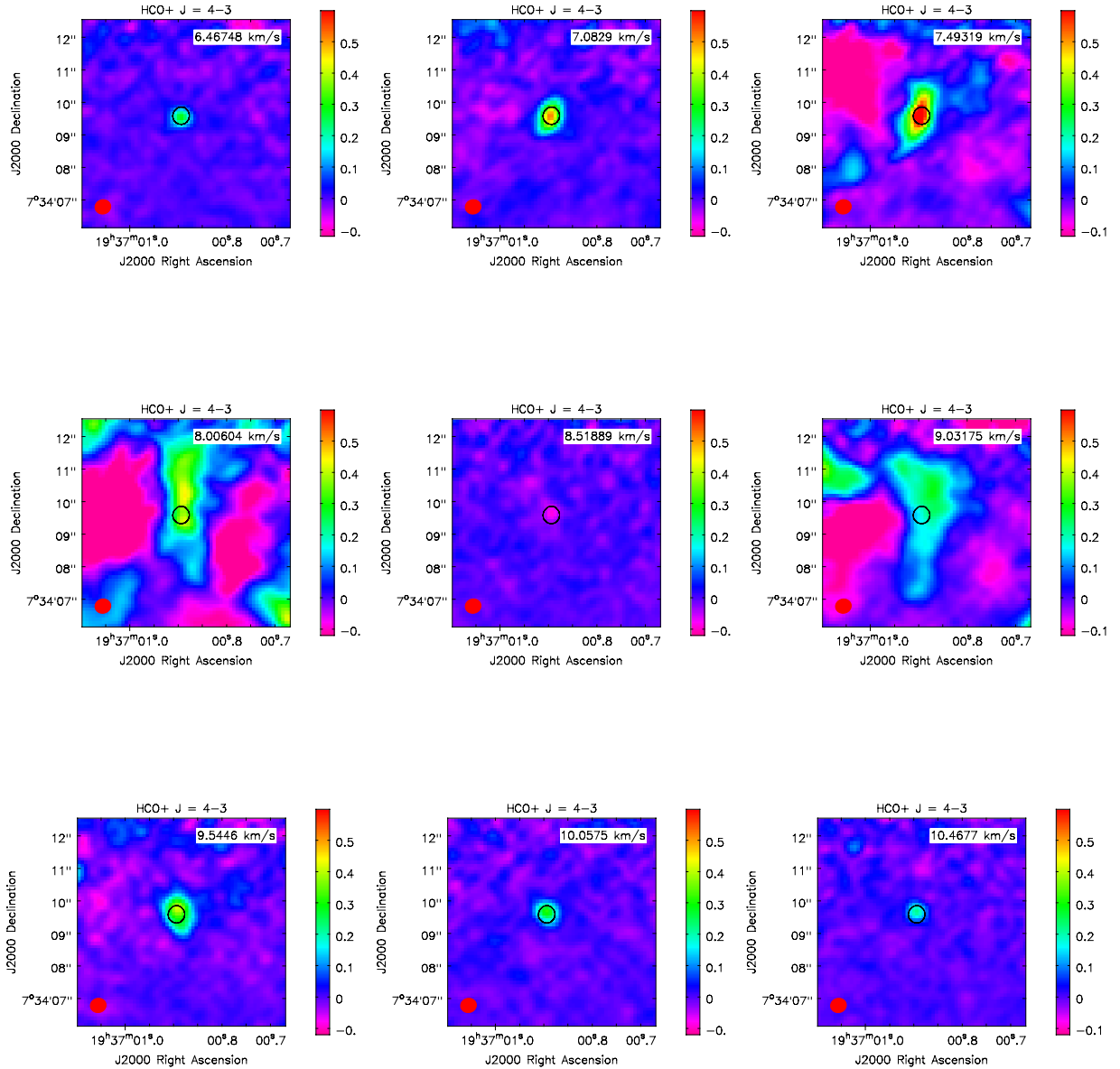


FIG. 2.— Channel maps of  $\text{HCO}^+$  toward B335, spaced by  $0.5 \text{ km s}^{-1}$ , after Hanning smoothing to an effective resolution of  $0.2 \text{ km s}^{-1}$ . The intensity range runs from  $-0.12 \text{ Jy/beam}$  to  $0.6 \text{ Jy/beam}$  and scaling power cycle was set to  $-0.2$  to display negative intensity as purple. Rainbow 1 color scheme in CASA was used. The red ellipse at lower left is the beam and the black ellipse near center is the half-power contour for the continuum emission.

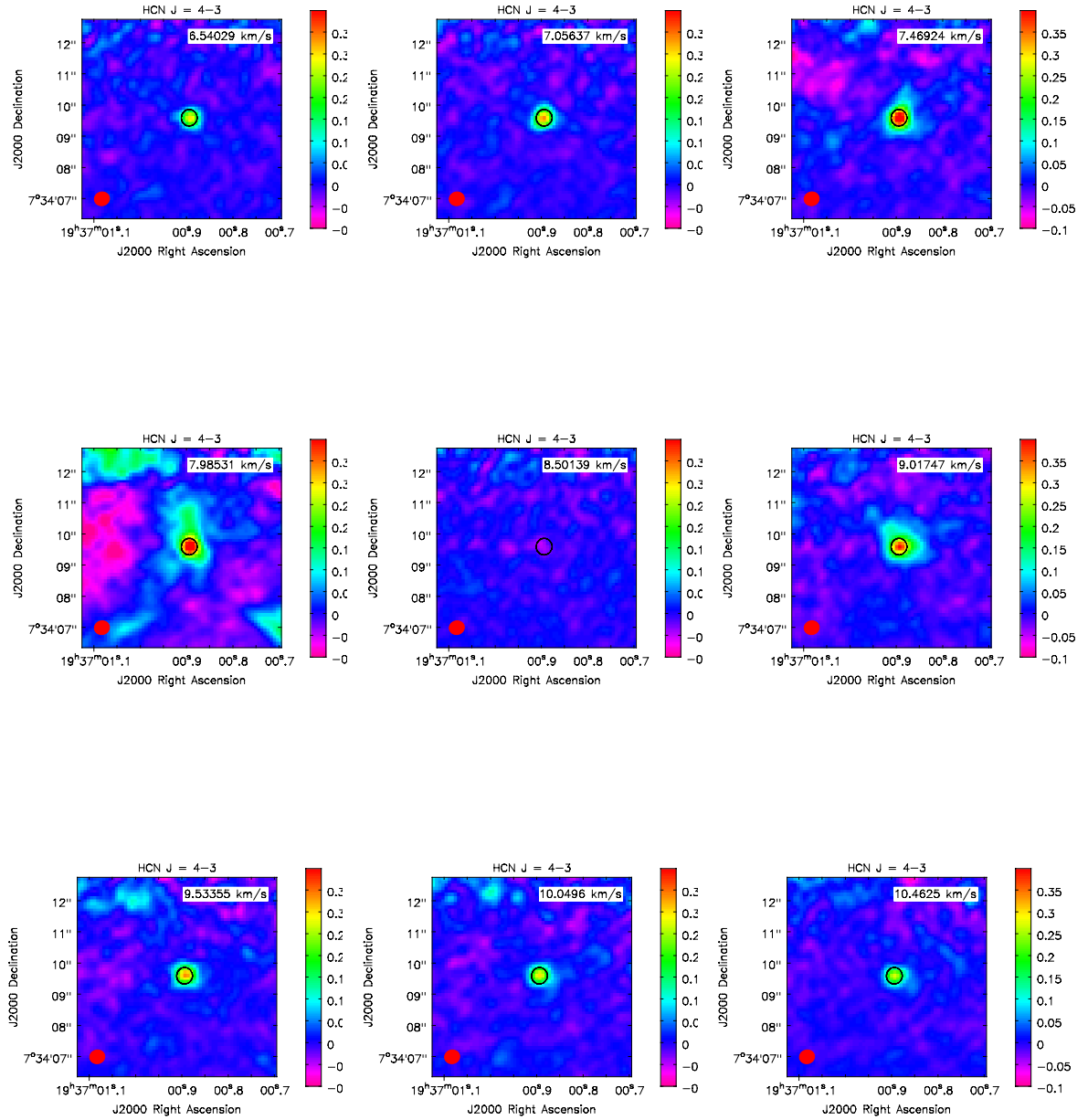


FIG. 3.— Channel maps of HCN toward B335, spaced by  $0.5 \text{ km s}^{-1}$ , after Hanning smoothing to an effective resolution of  $0.2 \text{ km s}^{-1}$ . The intensity range runs from  $-0.12 \text{ Jy/beam}$  to  $0.6 \text{ Jy/beam}$  and scaling power cycle was set to  $-0.2$  to display negative intensity as purple. Rainbow 1 color scheme in CASA was used. The red ellipse at lower left is the beam and the black ellipse near center is the half-power contour for the continuum emission.

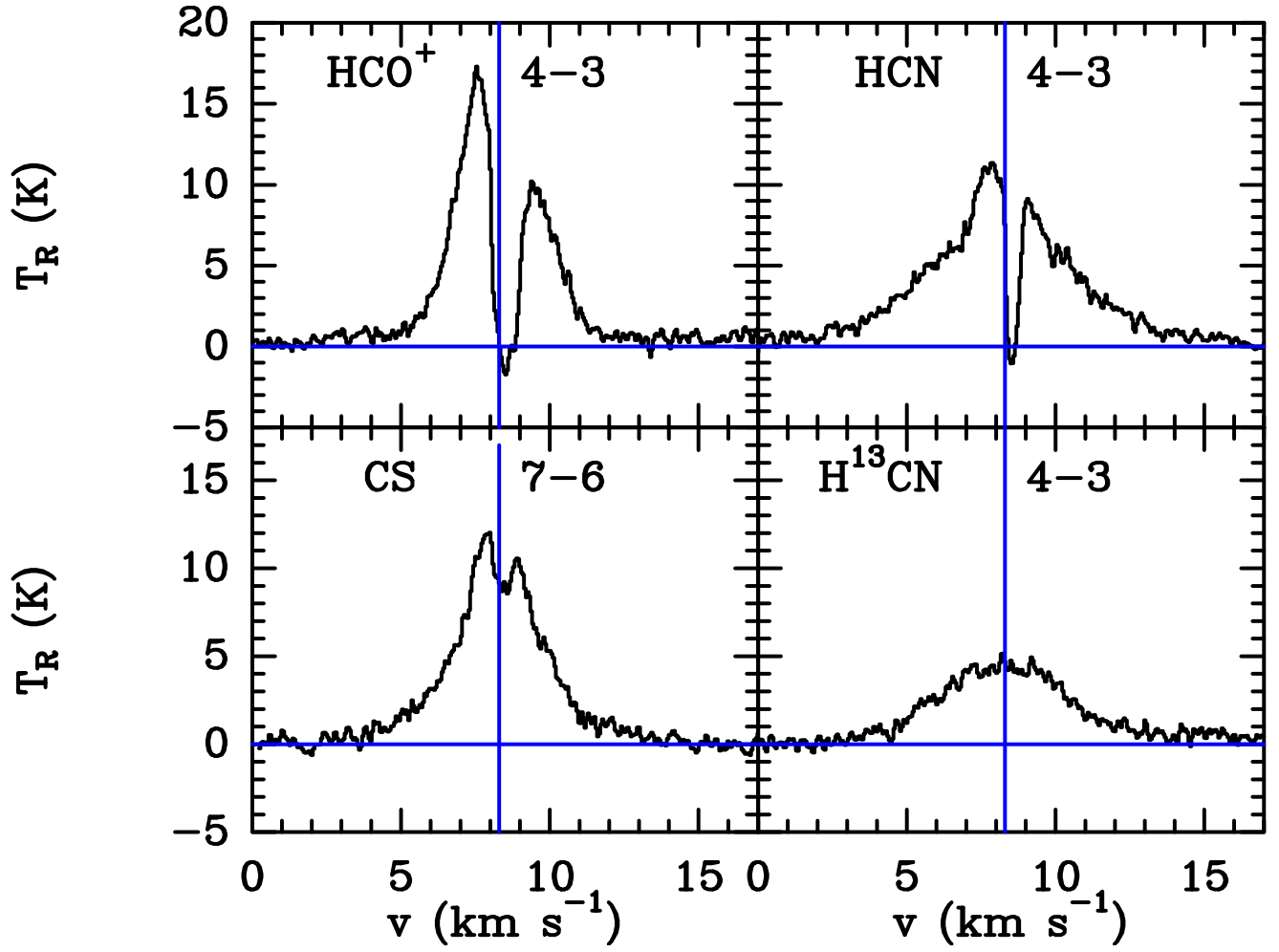


FIG. 4.— Spectra toward the continuum peak, after continuum subtraction, and scaling to the  $T_R$  scale. The blue horizontal line is at zero and the blue vertical line indicates the systemic velocity of  $8.30 \text{ km s}^{-1}$  found by Evans et al. (2005).

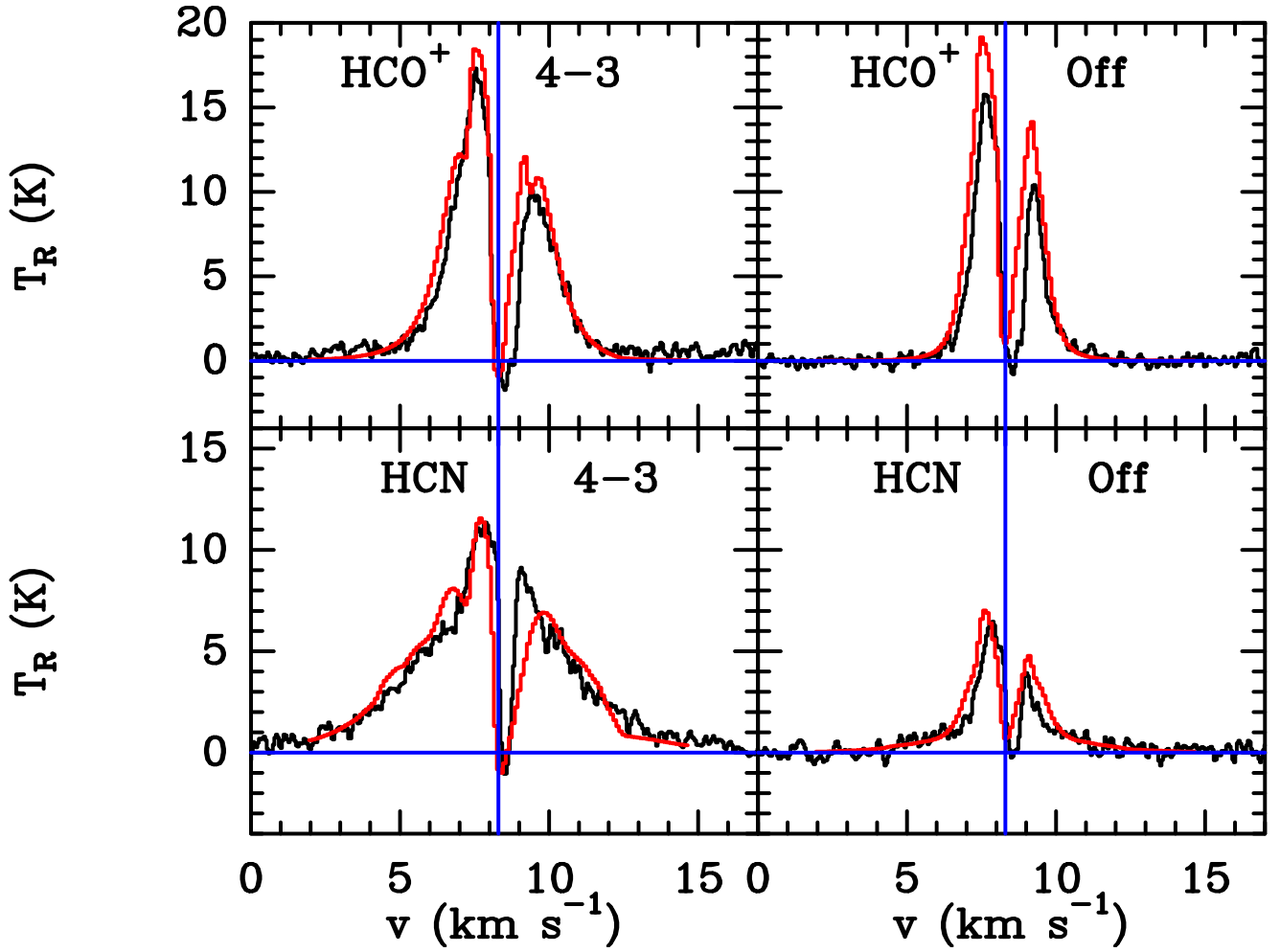


FIG. 5.— Models (red lines) of the lines for  $\text{HCO}^+$  and HCN are shown on top of the observed (black lines) profiles. The observations on the left are for centered spectra, while those on the right are the average of two positions, north and south by  $0''.5$  of the peak. The model is for a spherical inside-out collapse with  $r_{\text{inf}} = 0.012$  pc and abundance profiles in Table 2. The blue horizontal line is at zero and the blue vertical line indicates the systemic velocity.